Silicon Photonic Crystal Nanocavity-Coupled Waveguides for Error-Corrected Optical Biosensing

Sudeshna Pal[a,*], **Elisa Guillermain**[a], **Rashmi Sriram**[b], **Benjamin L. Miller**[b,c], and **Philippe M. Fauchet**[a,b]

[a] Dept. of Electrical and Computer Engineering, University of Rochester, Rochester, NY 14627, USA

[b] Dept. of Biomedical Engineering, University of Rochester, Rochester, NY 14627

[c] Dept. of Dermatology, University of Rochester, Rochester, NY 14627

Abstract

A photonic crystal (PhC) waveguide based optical biosensor capable of label-free and error-corrected sensing was investigated in this study. The detection principle of the biosensor involved shifts in the resonant mode wavelength of nanocavities coupled to the silicon PhC waveguide due to changes in ambient refractive index. The optical characteristics of the nanocavity structure were predicted by FDTD theoretical methods. The device was fabricated using standard nanolithography and reactive-ion-etching techniques. Experimental results showed that the structure had a refractive index sensitivity of 10^{-2} RIU. The biosensing capability of the nanocavity sensor was tested by detecting human IgG molecules. The device sensitivity was found to be $2.3 \pm 0.24 \times 10^5$ nm/M with an achievable lowest detection limit of 1.5 fg for human IgG molecules. Additionally, experimental results demonstrated that the PhC devices were specific in IgG detection and provided concentration-dependent responses consistent with Langmuir behavior. The PhC devices manifest outstanding potential as microscale label-free error-correcting sensors, and may have future utility as ultrasensitive multiplex devices.

Keywords

photonic crystal; nanocavity; optical biosensor; label-free; silicon

1. Introduction

Rapid, sensitive, redundant (error-corrected), and multiplexed detection of biological molecules is becoming increasingly important to progress in fields as diverse as basic biology, clinical diagnostics, biosecurity, and food and environmental safety. While technologies such as the real-time polymerase chain reaction, the enzyme-linked immunosorbent assay (ELISA), DNA microarrays and other methods reliant on a label such as a fluorophore or enzyme for readout are in wide use, they often require expensive equipment and are operationally complex (Lazcka et al., 2007). Thus, considerable research

*Correspondence to: Dr. Sudeshna Pal, pal@ece.rochester.edu, Ph: (585) 275 1768, Fax: (585) 276 2178.

effort continues to be directed towards label-free optical biosensing platforms as inexpensive and powerful biodetection tools.

A subset of the label-free optical biosensing approaches that have been described in the literature includes surface plasmon resonance (SPR), ring resonators, interferometer based methods, optical fibers and waveguides (Armani et al., 2007; Piliarik et al., 2005; Skivesen et al., 2007; Xu et al., 2007; Ymeti et al., 2006). These optical sensing techniques are heavily dependent on the evanescent field produced by optical waves to detect surface bound biological interactions based on local refractive index (RI) changes. The conventional SPR sensing that uses propagating surface plasmon polaritons on thin metallic films is perhaps the most intensely explored optical sensing technique in the literature (Homola, 2008). Detection limits in ng/ml and pg/mm^2 have been reported using conventional SPR and interferometric methods for different proteins (Fan et al., 2008; Homola et al., 2008). In a different approach, label-free optical biosensing has been performed using direct waveguide modes instead of evanescent modes in high pore density porous silicon waveguides in the Kretschmann configuration (Saarinen et al., 2005; Rong et al., 2008). Despite their versatility, most implementations of these optical techniques require large sensing areas and relatively large volumes of analytes, thus far limiting their applications in chip-based detection.

An emerging optical sensing technique that can be implemented with a small footprint and requires a small sample volume is the nanoplasmonic sensor. Nanoplasmonic sensors are based on nonpropagating localized surface plasmons (LSPRs) in nanostructured metals such as nanoparticles and nanoholes. These LSPRs can be resonantly excited, and are very sensitive to the refractive index of the dielectric medium (Stewart et al., 2008; Sepulveda et al., 2009). Detection limits in pg/cm^2 for different proteins have been achieved with these plasmonic sensors (Chen et al., 2009; Sannomiya et al., 2009). However, the low probe penetration depth and limited shelf life of the nanoplasmonic sensors restrain their application in detecting a wide range of analytes (Kabashin et al., 2009; Anker et al., 2008).

Photonic crystals (PhCs) are periodic dielectric structures that have recently emerged as promising alternatives to the above existing label-free optical sensing technologies. Our laboratories and others have provided thorough demonstrations of the utility of various one-dimensional PhC nanostructures as optical biological and chemical sensors (Chan et al., 2001; Cunin et al., 2002; Ouyang et al., 2005; Schwartz et al., 2006; Ouyang et al., 2007; Mandal and Erickson, 2008; Fan et al., 2008). In an effort to develop ultra-compact optical sensors with even higher sensitivity and with ultra-low sample volume capability, we have recently initiated a program to explore the sensing capabilities of two-dimensional (2D) PhC nanostructures fabricated in silicon. These devices exhibit a tunable photonic band gap (PBG) that has the ability to confine light in very small regions on the order of one wavelength or smaller. Photon confinement is achieved horizontally through the 2D PBG and vertically through total internal reflection (Joannopoulos et al., 1995; Kwon et al., 2008). Nano/micro cavities are formed in 2D PhC nanostructures by introducing point defects that break the crystal periodic lattice. The strong electric field confinement and small modal volumes (of the order of 0.1 μm^3) associated with such PhC nano/micro cavities make them very sensitive to local refractive index changes and suitable for ultra-small analyte volumes. Their ultra-small dimensions (in the order of microns) make 2D PhCs ideally suited for integration into compact footprints for on-chip biosensing applications.

Previously, several different configurations of 2D PhCs have been reported in the context of biosensing. Rindorf et al. have described the ability of long-period gratings in PhC fibers to detect biomolecules (Rindorf et al., 2006). PhC waveguide biosensors based on waveguide mode cut-off red-shifts have been investigated for specific detection of proteins (Buswell et

al., 2008). Cunningham and coworkers have demonstrated a polymer based PhC comprised of 1-D periodic grating surface structure for detection of viruses and protein-protein interactions (Heeres et al., 2009; Pineda et al., 2009). Similarly, different architectures of 2D PhC nano/micro cavities have also been exploited in biosensing applications (Chow et al., 2004; Dorfner et al., 2009; Lee and Fauchet, 2007b). Many of these cavity nanostructures are fabricated on silicon-on-insulator chips using nanofabrication techniques. Ultra-low detection limits in the range of femtograms of proteins and single particles have been demonstrated with such nanocavity structures (Lee and Fauchet, 2007a; Lee and Fauchet, 2007b).

The PhC nano/micro cavity designs discussed above, although extremely sensitive, are limited to detecting single analytes. When multiple such PhC cavity structures are placed in series, the resonance from the first PhC structure is not easily detected as it exists within the photonic bandgap of the adjacent PhC structure which prevents redundant as well as multiplexed detection. Devices capable of redundant biological detection (more than one sensor area responds to an analyte of interest) as an error-checking mechanism, or multiplex detection (multiple sensor areas capture different analytes) are of considerable interest. For sensitive and label-free biosensing, a PhC nanocavity structure with low mode volume, high quality factor and error-corrected or multiplex detection ability is preferred (Mandal and Erickson, 2008). We have designed and fabricated a nanocavity-coupled PhC waveguide nanostructure that has multiplexing capability, while maintaining the high sensitivity of the nanocavity device (Guillermain and Fauchet, 2009; Pal et al., 2010). In this paper, we simulate the response of this novel sensor and experimentally demonstrate its performance in refractive index sensing and in recognition-driven error-corrected biosensing of human IgG molecules.

2. Experimental

2.1. PhC device design

The 2D PhC slab structure designed for the biosensing experiments was based on silicon, and consisted of a 25×26 array of air holes in a triangular-lattice pattern (Figure 1a). A w1 waveguide (waveguide created by removing one row of air holes) was formed in the PhC structure by removing a central single row of air holes from the lattice (Liu et al., 2009). Nanocavities were created by reducing the radius of a single air hole adjacent to the w1 waveguide. The PhC devices had lattice constants (*a*) of 372, 380 and 388 nm and a Si slab thickness of ~ 400 nm, in order to have resonance in the wavelength ranges of 1440 and 1590 nm. The air hole radii were fixed at 111, 114 and 117 nm, while the corresponding defect diameters were kept at 73, 75 and 77 nm, respectively. The resonant modes of the photonic structures were modeled by 2D finite-difference- time-domain (FDTD) methods using the open source FDTD software Meep (Oskooi et al., 2010).

2.2. Device fabrication

The PhC devices were fabricated on a *p*-type silicon-on insulator (SOI) wafers (<100>) using electron beam lithography and reactive-ion etching. The SOI substrate had a 400 nm thick top device layer and a 1 μm thick buried oxide layer. A 130 nm thick oxide hard mask layer was thermally grown on the Si substrate by a wet oxidation process. Polymethylmethacrylate was then coated on the oxidized substrate as a soft etching mask to write high resolution PhC patterns using an e-beam writing system. After pattern writing and developing, the oxide hard mask layer was dry etched using argon assisted CHF_3 gas to transfer the patterns into the hard mask. The underlying Si device layer was etched using a gas mixture of CF_4 and BCl_3. After completion of the etching process, the PhC devices were

diced and the waveguide facets of the sensor chips were polished for coupling light from an external source. Figure 1b illustrates the fabrication process.

2.3. Optical detection

The spectral properties of the photonic devices were measured using a tunable laser (Hewlett Packard, model 8168F, output power: −7 to 7 dBm) in the wavelength range of 1440 to 1590 nm, with a wavelength resolution of 0.001 nm. Figure 1c shows a schematic of the measurement setup. Light from the laser source was transmitted through a polarization controller to excite the TE modes and coupled through tapered ridge waveguides into the PhC device using a tapered lensed fiber (Nanonics, Israel). The optical power transmitted through the device was collected via a second tapered lensed fiber and measured using an Indium Gallium Arsenide (InGaAs) photodiode detector (Teledyne Judson Technologies, PA, USA).

2.4. Sensor surface functionalization

Prior to any surface chemistry, dry thermal oxidation was conducted on the sensor chips at 900 °C for 15 min. The sensor surface functionalization was performed following a previously published protocol (Yadav et al., 2010). Details of the procedure have been outlined in the supplemental information where Figure S1 shows a schematic of the sensor surface functionalization and target binding.

2.5. Label-free target detection and spectroscopic ellipsometry

For optical detection, the antibody modified sensor chips were incubated with increasing concentrations of the target solution (human IgG) diluted in PBS buffer modified with 0.005% Tween 20 in a humidity chamber at room temperature overnight. Subsequently, the chips were rinsed with distilled deionized water to remove unbound targets and dried under a stream of nitrogen before performing optical measurements. To determine the selectivity of the biosensor, the chips were incubated with 15 μM bovine serum albumin (BSA), a non-target protein, diluted in buffer. The spectral responses were recorded after subsequent washing with distilled deionized water and drying of the chips under a stream of nitrogen.

The chemical and protein-layer thickness measurements were carried out on p-type planar silicon chips (<100>). After subsequent chemical or protein treatment, the thickness measurements were made on dried chips using a spectroscopic ellipsometer at an incident angle of 70°. The measured thickness values were accurate within ± 0.1 Å.

3. Results and Discussion

3.1. Simulations

The periodicity of the triangular pattern of air holes in a 2D PhC slab results in the formation of a photonic bandgap. Removal of a line of air holes in the crystal structure creates a w1 PhC waveguide structure resulting in waveguide modes within the photonic band gap (Liu et al., 2009). The guided modes are strongly confined in the Si layer by the lower refractive index contrasts (with air and SiO_2) in the vertical direction. A single nanocavity coupled PhC device having a defect radius of 0.15a and air hole radii of 0.3a was modeled using the finite-difference time domain (FDTD) method. This method computes light propagation in the PhC structure by solving Maxwell's equations for electromagnetic waves in both time and space coordinates. The computational space is sampled at very small intervals of all wavelengths under consideration, and the material properties are specified at each sample point. The method is appropriate for computing field distributions and resonance decay times (quality factor Q) and is advantageous since response at all frequencies can be

obtained by sending a pulse into the structure and also permits analysis of large irregular structures in addition to periodic structures (Prather et al., 2009).

The simulated spectrum for the single nanocavity PhC waveguide structure in Figure 2a shows high light transmission through the waveguide at all frequencies except at the resonant mode of the nanocavity, where a sharp dip in transmission is observed. The calculated normalized resonant frequency f (f = a/λ, where λ = vacuum wavelength) of the nanocavity was 0.264. The Q-factor, defined as $\omega_0/\Delta\omega$ (ω_0 = resonant frequency), was calculated to be 450. Figure 2b shows the simulated electric field distribution ($|E|^2$) in the structure at the resonant frequency. The strong field confinement in the nanocavity region as seen in the figure suggests that due to enhanced light-matter interaction in the defect hole, the structure is extremely sensitive to local refractive index changes.

The error-correcting or multiplexing capability of the PhC waveguide design was assessed by modeling a PhC structure where two nanocavities were coupled to the same PhC waveguide having defect radii of 0.15a and 0.18a. The hole radius was fixed at 0.3a. The simulated transmission spectrum (Figure 2c) for the above structure shows two transmission dips at normalized resonant frequencies of 0.264 and 0.268 which correspond to the resonant mode of each nanocavity. The calculated Q-factors for each nanocavity are 400 and 850, respectively. The electric ($|E|^2$) field profiles in Figures 2d and 2e show strong field confinement at the resonant frequency of each nanocavity. The simulation results thus indicate that each nanocavity coupled to the PhC waveguide can perform as an independent biosensor when functionalized with different biomolecules.

3.2. RI sensing with single nanocavity coupled devices

The fabricated PhC waveguide devices were investigated for RI sensing with water (n = 1.33) and isopropanol (n = 1.377). Figure 3a shows the SEM image of a fabricated single nanocavity-coupled PhC waveguide device having a lattice constant of 380 nm, hole radius of 114 nm and defect radius of 75 nm. The fabricated structure showed slight deviations in the lattice constants and in the hole and defect dimensions from the above mentioned values; these deviations may be attributed to minor imperfections in the fabrication process. The above structure had an experimental resonance dip at ~ 1532 nm in air (n = 1.0) as seen in Figure 3b. The net red-shifts in the resonant wavelength of the nanocavity ($\delta\lambda$) in water and isopropanol (IPA) were 21 nm and 24.6 nm, respectively, due to the increase in RI inside the holes. The RI sensitivity of the device was calculated to be 64.5 nm/RIU ($\delta\lambda/\delta n$) or 10^{-2} RIU ($\delta n/n$) which is within the sensitivity range of other PhC nanocavity sensors (10^{-2} to 10^{-4} RIU) reported in literature (Dorfner et al., 2008; Fan et al., 2008; Falco et al., 2009). While the RI sensitivities of PhC devices are lower than most SPR based sensing techniques (10^{-5} to 10^{-8} RIU) (Fan et al., 2008), SPR requires a much larger detection area in SPR than PhC devices. The measured mode Q-factor of the nanocavity when infiltrated with liquid (Q_{IPA} = 457, Q_{water} = 409) is lower than that in air (Q_{air} = 479) due to higher in-plane losses into the PhC waveguide. The RI sensitivity of the PhC nanocavity sensor can be further improved by designing and fabricating devices with higher Q-factors.

3.3. IgG sensing with multiple nanocavity coupled devices

The detection of IgG by sensors functionalized with anti-IgG antibodies was used to evaluate the performance of the nanocavity coupled PhC waveguide devices. Figure 4a shows the SEM image of a fabricated device where three nanocavity coupled PhC waveguides are placed in series. The defect radii were 73, 75 and 77 nm and the lattice constants were 372, 380 and 388 nm. The structure shows three transmission dips at 1510, 1531 and 1551 nm (Figure 4b) that correspond to the resonance mode of each nanocavity. The experimental Q-factors of the cavities varied from 300 to 500. To assess the

performance of the device, the receptor (anti-human IgG) functionalized device was treated with 6.7×10^{-6} M of the target solution (human-IgG). Figure 4b shows the transmission spectra of the device where the blue line indicates the baseline spectrum before surface functionalization and the red line indicates the final spectrum after IgG binding. A net red-shift of 3.5 nm was observed in each nanocavity, thus demonstrating for a single analyte of interest successful error-corrected (redundant) detection capability of the device. Our results also suggest that detecting different analytes on a single platform is possible when each nanocavity is functionalized with a different capture biomolecule.

Figure 5a shows the dose response curve of multiple defect PhC sensors in IgG concentrations ranging from 6.7×10^{-10} M to 6.7×10^{-6} M. The resonance red-shifts of the nanocavities observed for different concentrations of the IgG molecules were normalized with respect to the red-shifts observed in the negative control (PhC sensor chips immobilized with antibodies and treated with buffer solution alone). The biosensor response sharply increases with increasing IgG concentrations and tends to saturate at high concentrations. The normalized red-shifts change from 0.29 ± 0.11 nm for an IgG concentration of 6.7×10^{-9} M to 1.56 ± 0.24 nm for the highest tested IgG concentration of 6.7×10^{-6} M. The standard deviations in the sensor response are attributed to chip-to-chip differences in antibody immobilization efficiency, as well as variations in experimental Q factors of the nanocavities arising from fabrication imperfections. From Figure 5a, the sensitivity of the PhC device expressed as $\delta\lambda_{max}/C_{max}$ (where C_{max} is the saturation concentration) was calculated to be $2.3 \pm 0.24 \times 10^5$ nm/M.

The experimental resonance red-shifts were fitted with the Langmuir adsorption isotherm in order to estimate the binding affinity and dissociation constants of the IgG molecules (Duschl, 2002). Figure 5a (inset) shows the Langmuir fit curve based on the equation $\delta\lambda/\delta\lambda_{max} = K_A c/(1 + K_A c)$, where $\delta\lambda_{max}$ is the maximum red-shift observed at the saturation concentration ($\delta\lambda_{max} = 1.56$ nm), c is the IgG concentration and K_A is the association constant for antibody-protein pair. The K_A and dissociation constant ($K_D = 1/K_A$) for human-IgG and its antibody from Langmuir fits were 1.38×10^6 M^{-1} and 7.2×10^{-7} M, respectively. These thermodynamic constants determined from the PhC sensors are in agreement with the K_A (~ 10^6 to 10^7 M^{-1}) and K_D (~ 10^{-7} to 10^{-9} M) values reported in the literature for anti-IgG and IgG binding (Varghese et al., 2008; Welschof et al., 1997). These data suggest that operation of the PhC devices in a fluidic environment may allow them to be exploited in kinetic and equilibrium studies of biomolecular binding.

The specificity of the PhC sensor chips was evaluated by measuring responses in the presence of BSA, a protein that does not bind to the anti-IgG antibodies used in the detection experiments. Figure 5b shows a comparison of the normalized resonance red-shifts observed with the PhC devices tested for a 15×10^{-6} M BSA solution, the highest tested IgG concentration 6.7×10^{-6} M, and the negative control consisting of buffer alone. The sensor response for the BSA solution (normalized shift: 0.041 ± 0.3 nm) was similar to the response observed for negative control (buffer alone) and much smaller than the red-shift observed with the target solution. These results indicate that the PhC nanocavities can perform as a specific biosensing device.

FDTD simulations were performed in order to provide a theoretical benchmark against which the experimental results could be compared. A comparison of the experimental resonance red-shifts measured for the fabricated devices with the red-shifts predicted by the FDTD simulations is shown in Figure 6. The simulations were performed assuming layers of protein molecules coating the internal surface of the device with layer thicknesses ranging from 0 to 100 Å. An RI value of 1.5 was chosen for simulations based on reported RI of dried protein layers obtained from atomic force microscopy and ellipsometry (Benesch et

al., 2002; Vörös, 2004). The theoretical red-shift increased from 1.45 nm to 5.54 nm with increasing layer thickness from 20 to 100 Å. This linear increase in the red-shift value is expected as the sensing principle of the PhC waveguide structure is reliant on perturbations of the nanocavity mode confined in the lower dielectric (in air) instead of the higher dielectric (in silicon). As observed from previous field profile simulations (Fig. 2b), the resonant optical field exists inside the defect hole, i.e. in the lower dielectric, and hence allows enhanced light matter interaction in comparison to other PhC nanocavity sensor designs that are based on the short evanescent tail of optical waves (Dorfner et al., 2009) where the red-shifts are expected to saturate with increasing layer thicknesses in response to the decaying evanescent field. In Figure 6, the theoretical data are not precisely linear as the coating thicknesses were thinner than the grid size assumed in the simulations for the lower thicknesses. The average layer thicknesses determined by ellipsometric measurements were 17.8 Å for chemical functional groups (APDMES plus glutaraldehyde), 45 Å for anti-IgG immobilization (chemical layers + anti-IgG) and in the range of 52.6 to 63 Å for IgG binding (concentrations of 0.067×10^{-6} M, 0.67×10^{-6} M and 6.7×10^{-6} M). The corresponding experimental red-shifts observed in the PhC nanocavity devices were 1.06 ± 0.15, 1.98 ± 0.18 and from 2.54 ± 0.10 to 3.56 ± 0.24 nm, respectively. Figure 6 shows that the experimental red-shifts after chemical attachment and after IgG binding at the saturation concentration (6.7×10^{-6} M) match closely with the linear fit of the simulated theoretical curve thus indicating 100 % coverage of the sensor surface in both instances. The surface coverage was less than 100 % (in the range of 85 – 87 %) for anti-IgG immobilization and IgG binding at lower concentrations. Thus, it can be inferred that chemical crosslinking and IgG binding at the highest concentration result in uniform coating on the PhC nanocavity devices (as assumed in the FDTD simulations) and hence a close match in the experimental and simulated red-shift data is observed. However, the protein thicknesses after anti-IgG immobilization and IgG binding at lower concentrations are not as uniform as assumed in the simulations and hence lead to lower experimental red-shifts due to lower refractive index contrasts between silicon and the protein layer.

The detection limit of the PhC nanocavity device was calculated from the sensor red-shift response and protein thickness measurements. From Figure 5a, the lowest IgG concentration that resulted in a reliable red-shift having S/N ratio greater than 3.0 was 6.7×10^{-8} M. However, the actual mass of the proteins contributing to the biosensor signal was much less than what the above concentration would suggest. The FDTD simulations in Figure 2b showed that the electric field intensity was mostly confined ($> 50\%$) in the central defect and the surrounding four holes, indicating that the majority of the biosensor response was generated from this region. This "active" biosensing area of the PhC nanocavity device may be calculated considering the internal surface area of the pore walls of the above mentioned region and was found to be 1.465 μm^2. The surface density of the IgG molecules bound in this active region at the lowest detectable IgG concentration (6.7×10^{-8} M) was estimated to be 1 ng/mm^2 from the protein monolayer thickness measurements and the protein density values (Shumaker-Parry and Campbell, 2004). The mass of the IgG molecules in the active region that produced a measurable red-shift was 1.5 fg, which was therefore the minimum detection limit of the PhC nanocavity device based on signal transduction limitations. This result was consistent with other PhC nanocavity sensors reported for protein detection in the literature that had experimental detection limits in the range of 2.5–4.0 fg (Dorfner et al., 2009; Lee and Fauchet, 2007b).

4. Conclusion

We have developed a silicon based 2-D PhC optical biosensor suitable for label-free and error-corrected (redundant) biosensing. The PhC sensor shows a RI sensitivity of 64.5 nm/ RIU (or 10^{-2} RIU) with liquids of different refractive indexes. We have also demonstrated

error-corrected biosensing of human IgG molecules using the PhC optical sensor. The device has a sensitivity of $2.3 \pm 0.24 \times 10^5$ nm/M and a detection limit of 1.5 fg for human IgG molecules. Experimental results indicate that the devices are good candidates for further development as multiplexed biosensors; achieving this will require addressing the challenge of independently addressing each nanocavity with a different biomolecular capture agent. Efforts to accomplish that goal are under way in our laboratories. The performance of the biosensor can be further improved by designing nanocavities having higher quality factors and by localizing the biomolecular recognition processes in the defect feature. Future work shall also involve performing real-time measurements with the devices in fluidic environment.

Supplementary Material

Refer to Web version on PubMed Central for supplementary material.

Acknowledgments

References

Anker JN, Hall WP, Lyandres O, Shah NC, Zhao J, Van Duyne RP. Nature Materials. 2008; 7(6):442–453.

Armani AM, Kulkarni RP, Fraser SE, Flagan RC, Vahala KJ. Science. 2007; 317(5839):783–787. [PubMed: 17615303]

Benesch J, Askendal A, Tengvall P. Journal of Colloid and Interface Science. 2002; 249(1):84–90. [PubMed: 16290571]

Buswell SC, Wright VA, Buriak JM, Van V, Evoy S. Optics Express. 2008; 16(20):15949–15957. [PubMed: 18825232]

Chan S, Horner SR, Fauchet PM, Miller BL. Journal of the American Chemical Society. 2001; 123(47):11797–11798. [PubMed: 11716737]

Chen S, Svedendahl M, Käll M, Gunnarsson L, Dmitriev A. Nanotechnology. 2009; 20(43):434015. [PubMed: 19801769]

Chow E, Grot A, Mirkarimi LW, Sigalas M, Girolami G. Optics Letters. 2004; 29(10):1093–1095. [PubMed: 15181996]

Cunin F, Schmedake TA, Link JR, Li YY, Koh J, Bhatia SN, Sailor MJ. Nature Materials. 2002; 1:39–41.

Di Falco A, O'Faolain L, Krauss TF. Applied Physics Letters. 2009; 94(6):063503–1.

Dorfner D, Zabel T, Hnrlimann T, Hauke N, Frandsen L, Rant U, Abstreiter G, Finley J. Biosensors and Bioelectronics. 2009; 24(12):3688–3692. [PubMed: 19501502]

Duschl, C. Biomolecular Sensors. Taylor and Francis; London: 2002.

Fan X, White IM, Shopova SI, Hongying Z, Suter JD, Sun Y. Analytica Chimica Acta. 2008; 620(1–2):8–26. [PubMed: 18558119]

Guillermain, E.; Fauchet, PM. Proceedings of SPIE 7167. 2009. p. 71670D-1

Heeres JT, Kim SH, Leslie BJ, Lidstone EA, Cunningham BT, Hergenrother PJ. Journal of the American Chemical Society. 2009; 131(51):18202–18203. [PubMed: 19968284]

Homola J. Chemical Reviews. 2008; 108(2):462–493. [PubMed: 18229953]

Joannopoulos, JD.; Meade, RD.; Winn Joshua, N. Photonic Crystals: Molding the Flow of Light. Princeton University Press; 1995.

Kabashin AV, Evans P, Pastkovsky S, Hendren W, Wurtz GA, Atkinson R, Pollard R, Podolskiy VA, Zayats AV. Nature Materials. 2009; 8(11):867–871.

Kwon SH, Snnner T, Kamp M, Forchel A. Optics Express. 2008; 16(16):11709–11717. [PubMed: 18679440]

Lazcka O, Del Campo FJ, Munoz FX. Biosensors & Bioelectronics. 2007; 22(7):1205–1217. [PubMed: 16934970]

Lee MR, Fauchet PM. Optics Letters. 2007a; 32(22):3284–3286. [PubMed: 18026281]

Lee M, Fauchet PM. Optics Express. 2007b; 15(8):4530–4535. [PubMed: 19532700]

Liu K, Yuan XD, Ye WM, Zeng C. Optics Communications. 2009; 282(22):4445–4448.

Mandal S, Erickson D. Optics Express. 2008; 16(3):1623–1631. [PubMed: 18542241]

Oskooi AF, Roundy D, Ibanescu M, Bermel P, Joannopoulos JD, Johnson SG. Computer Physics Communications. 2010; 181(3):687–702.

Ouyang H, Cristophersen M, Viard R, Miller BL, Fauchet PM. Advanced Functional Materials. 2005; 15(11):1851–1859.

Ouyang H, DeLouise LA, Miller BL, Fauchet PM. Analytical Chemistry. 2007; 79(4):1502–1506. [PubMed: 17241093]

Pal S, Guillermain E, Sriram R, Miller B, Fauchet PM. Proceedings of SPIE. 2010; 7553:755304–1.

Piliarik M, Vaisocherovβ H, Homola J. Biosensors and Bioelectronics. 2005; 20(10):2104–2110. [PubMed: 15741081]

Pineda MF, Chan LLY, Kuhlenschmidt T, Choi CJ, Kuhlenschmidt M, Cunningham BT. Sensors Journal, IEEE. 2009; 9(4):470–477.

Prather, DW.; Shi, S.; Sharkawy, A.; Murakowski, J.; Schneider, GJ. Photonic Crystals: Theory, Applications and Fabrication. John Wiley & Sons, Inc; 2009.

Rindorf L, Jensen JB, Dufva M, Pedersen LH, Hoiby PE, Bang O. Optics Express. 2006; 14(18):8224–8231. [PubMed: 19529196]

Rong G, Ryckman JD, Mernaugh RL, Weiss SM. Applied Physics Letters. 2008; 93(16):161109–3.

Saarinen JJ, Weiss SM, Fauchet PM, Sipe JE. Optics Express. 2005; 13(10):3754–3764. [PubMed: 19495282]

Sannomiya T, Sahoo PK, Mahcices DI, Solak HH, Hafner C, Grieshaber D, Vörös J. Small. 2009; 5(16):1889–1896. [PubMed: 19384877]

Sepulveda B, Angelome PC, Lechuga, Liz-Marzan LM. Nano Today. 2009; 4(3):244–251.

Schwartz MP, Derfus AM, Alvarez SD, Bhatia SN, Sailor MJ. Langmuir. 2006; 22(16):7084–7090. [PubMed: 16863264]

Shumaker-Parry JS, Campbell CT. Analytical Chemistry. 2004; 76(4):907–917. [PubMed: 14961720]

Skivesen N, Horvath R, Thinggaard S, Larsen NB, Pedersen HC. Biosensors and Bioelectronics. 2007; 22(7):1282–1288. [PubMed: 16828273]

Stewart ME, Anderton CR, Thompson LB, Maria J, Grey SK, Rogers JA, Nuzzo RG. Chemical Reviews. 2008; 108(2):494–521. [PubMed: 18229956]

Varghese LT, Sinha RK, Irudayaraj J. Analytica Chimica Acta. 2008; 625(1):103–109. [PubMed: 18721546]

Vörös J. Biophysical Journal. 2004; 87(1):553–561. [PubMed: 15240488]

Welschof M, Terness P, Kipriyanov SM, Stanescu D, Breitling F, Dörsam H, Dübel S, Little M, Opelz G. Proceedings of the National Academy of Sciences. 1997; 94(5):1902–1907.

Xu F, Horak P, Brambilla G. Optics Express. 2007; 15(12):7888–7893. [PubMed: 19547115]

Yadav AR, Sriram R, Miller B. Proceedings of SPIE. 2010; 7553:75530J.

Ymeti A, Greve J, Lambeck PV, Wink T, van H, Beumer, Wijn RR, Heideman RG, Subramaniam V, Kanger JS. Nano Letters. 2006; 7(2):394–397. [PubMed: 17298006]
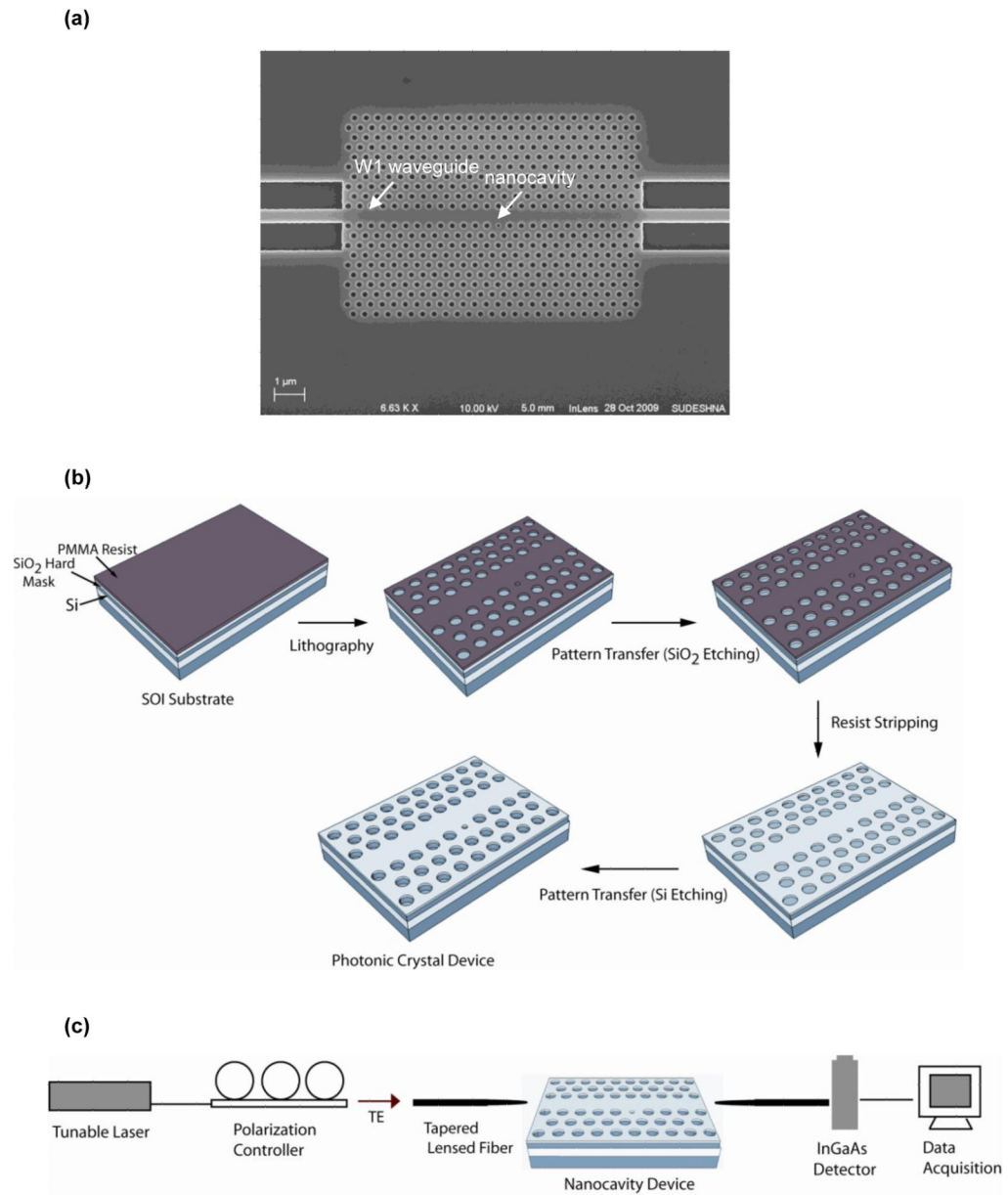
(a)

(b)

(c)

Figure 1.
(a) SEM image of a fabricated PhC nanocavity device (b) Schematic illustration of the fabrication process and (c) The optical detection setup.
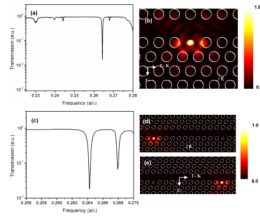
Figure 2.
(a) Simulated transmission spectrum of a PhC nanocavity structure having a defect radius of 0.15 *a* coupled to a w1 PhC waveguide. The excitation is TE polarized at normalized frequency f = a/λ, where λ = vacuum wavelength, (b) Simulated electric ($|E|^2$) field profile for the resonant frequency of the structure in air, (c) Simulated transmission spectrum of a structure with two nanocavities coupled to a w1 PhC waveguide, (d) Simulated $|E|^2$ field profile for the resonant frequency of the first defect in air (e) Simulated ($|E|^2$) field profile for the resonant frequency of the second defect in air.
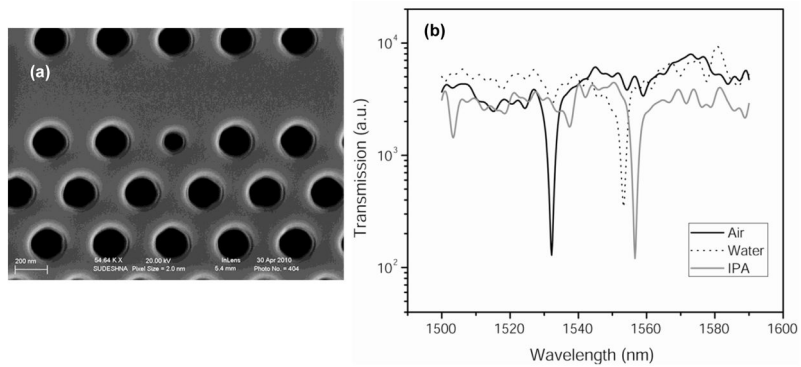
Figure 3.
(a) SEM image of a fabricated single defect PhC device (a = 380 nm, defect radius = 75 nm), (b) Experimental transmission spectra of the device in air, water and isopropyl alcohol.
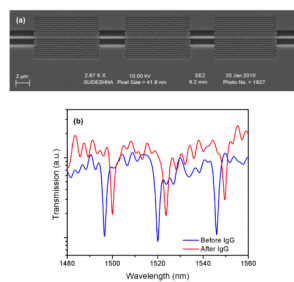
Figure 4.
(a) SEM image of fabricated multiple nanocavity coupled PhC devices (*a* = 372, 380 and 388 nm, defect radius = 73, 75 and 77 nm) in series (b) Experimental transmission spectra of the structure before and after target (IgG) binding.
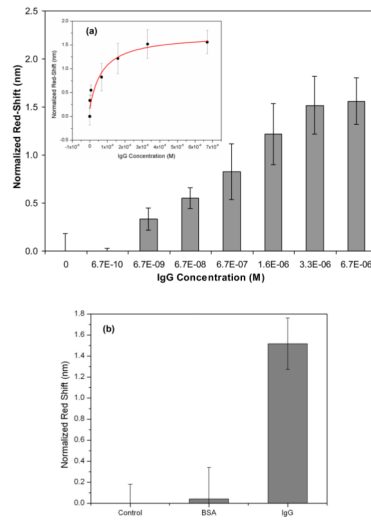
Figure 5.
(a). Experimental normalized red-shifts of the PhC nanocavity device vs. increasing concentrations of IgG molecules, Inset- Langmuir fit of the data, $R^2 = 0.9214$ (b) Specificity response of the PhC nanocavity device. Error bars are represented as average normalized red shift ± standard deviation for n = 5.
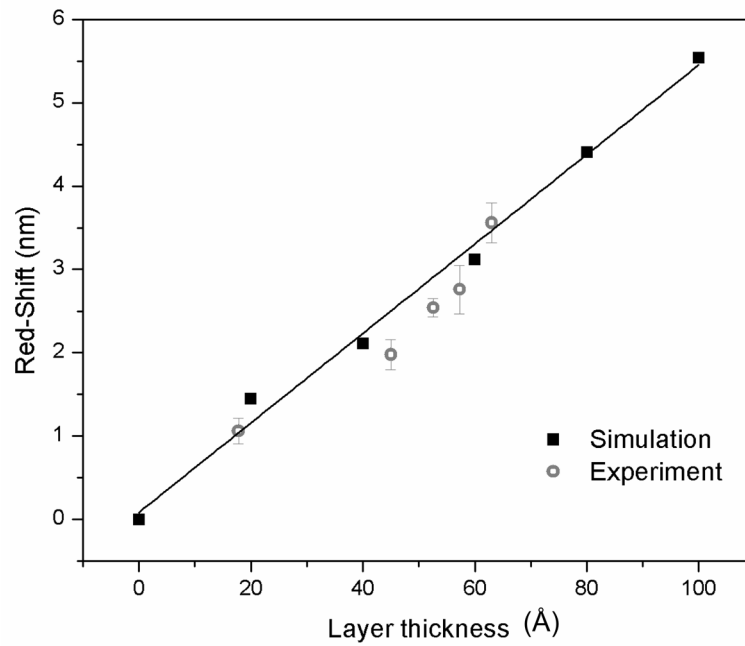
Figure 6.
Theoretical and experimental responses of the multiple defect PhC nanocavity device for different thicknesses of proteins layers and chemical crosslinkers. The black solid line corresponds to a linear fit to the predicted thickness values. R^2 for the fit was 0.9908. Error bars are represented as average normalized red shift $\pm$ standard deviation for n = 5.